remote sensing

MDPI

Article

Monitoring Damage Caused by *Pantana phyllostachysae* Chao to Moso Bamboo Forests Using Sentinel-1 and Sentinel-2 Images

Xuying Huang [1,2,3], Qi Zhang [3], Lu Hu [1,2], Tingting Zhu [1,2], Xin Zhou [3], Yiwei Zhang [3], Zhanghua Xu [3] and Weimin Ju [1,4,*]

1 International Institute for Earth System Science, Nanjing University, Nanjing 210023, China
2 School of Geography and Ocean Science, Nanjing University, Nanjing 210023, China
3 Academy of Geography and Ecological Environment, Fuzhou University, Fuzhou 350108, China
4 Jiangsu Center for Collaborative Innovation in Geographical Information Resource Development and Application, Nanjing 210023, China
* Correspondence: juweimin@nju.edu.cn

Abstract: *Pantana phyllostachysae* Chao (PPC) is one of the deadliest defoliators of Moso bamboo. Accurately locating and evaluating PPC damage is essential for the management of bamboo forests. Moso bamboo has a unique biennial growth cycle, consisting of the on-year period (bamboo shoots are incubated and then produced) and the off-year period (old leaves are dropped and then new leaves are grown, and no bamboo shoots are produced in the coming year). The similar physiological characteristics of off-year bamboo and damaged on-year bamboo create difficulties in monitoring PPC damage using remote sensing data. In this study, we synergistically used Sentinel-1, Sentinel-2, and field inventory data to construct machine learning (extreme gradient boosting, XGBoost) models monitoring PPC damage. The results show that the single-time observation feature-based model (using images from October) outperformed the double-time observation feature-based model (using the differences between remote sensing signals from October and February or April) due to the interference from other disturbance agents (e.g., logging and weeding). The overall accuracy (OA) values of the single-time observation feature-based model were at least 3% and 10% higher than those for double-time observation feature-based models for on- and off-year samples, respectively. With the consideration of the on- and off-year phenological differences, OA was improved by over 4%. The model without differentiation of the phenological difference tended to underestimate the damaged area of on-year bamboo and overestimate that of off-year bamboo. We also found that the responses of optical and SAR (synthetic aperture radar) features to PPC damage were different. The optical features increased or decreased with increasing damage severity. SAR features decreased significantly at the initial stage of PPC damage and then changed marginally with the increase in damage severity. The addition of SAR features to optical features improved the model performance, mainly for healthy and mildly damaged samples. The methodology developed in this study provides technical and theoretical support for the pest monitoring of bamboo forests using remote sensing data.

Keywords: insect disturbance; Moso bamboo; pest; remote sensing; machine learning

Citation: Huang, X.; Zhang, Q.; Hu, L.; Zhu, T.; Zhou, X.; Zhang, Y.; Xu, Z.; Ju, W. Monitoring Damage Caused by *Pantana phyllostachysae* Chao to Moso Bamboo Forests Using Sentinel-1 and Sentinel-2 Images. *Remote Sens.* **2022**, *14*, 5012. https://doi.org/10.3390/rs14195012

Academic Editor: Wenjiang Huang

Received: 25 August 2022
Accepted: 4 October 2022
Published: 8 October 2022

1. Introduction

Bamboo is an important ecological and economic forest type that is mainly distributed in Asia, South America, and Africa [1]. The area of bamboo forests in China is the largest globally and amounts to 6.41 million ha, of which the area of Moso bamboo (*Phyllostachys pubescens*) accounts for 72.96% of the total [2]. The harvest period of Moso bamboo is short, which ensures that farmers can obtain the benefits from various bamboo products every year. Therefore, the bamboo industry's economy is the main source of fiscal revenue in many regions. Bamboo production is also a critical project undertaken by the Chinese government and is intended to alleviate poverty in many poor mountainous areas. Additionally, bamboo

has a high carbon sequestration capacity and could make a considerable contribution to the terrestrial carbon sink [3].

However, the biodiversity of bamboo forests is commonly low because of bamboo's unique growth pattern (i.e., clonal reproduction and invasive expansion) and anthropogenic intervention in the forest structure [4]. Bamboo forests experience various insect disturbance events every year due to the lack of predators in the forests. There are more than 630 species of insects that threaten bamboo forests, of which *Pantana phyllostachysae* Chao (PPC) is the most destructive [5]. Its larvae mainly feed on bamboo leaves and are usually present three times each year, comprising the overwintering generation (from March to May), the first generation (from June to August), and the second generation (from September to November). After hatching, the larvae move from the trunk to the top of the canopy and attack leaves. The host's leaves are consumed quickly when the larval population accumulates to an epidemic level. The photosynthetic and nutrient transport efficiencies of the host are seriously weakened, and its resilience to secondary attacks is reduced. The host's physiological functions collapse after successive defoliation events, eventually leading to death. The shoot production of the host in the following year seriously decreases, and the material and volume of new bamboo in the damaged areas noticeably decline [6].

The topographic conditions of bamboo's habitat are usually complex, which imposes challenges in respect of manually monitoring PPC damage [7]. Data collected are usually not comprehensive and lack timeliness. Irreversible and extensive damage has already occurred by the time it is found. Therefore, an effective monitoring method is urgently needed for the better prevention of PPC.

Optical remote sensing, especially moderate-resolution optical remote sensing, provides an essential data basis for forest insect disturbance monitoring at large scales [8,9]. Spectral variation can be used to determine the damaged area and severity. Normally, the herbivorous behavior of defoliators results in the destruction of the leaf tissue structure, and leaf moisture will be lost from damaged edges [10]. When the wounds heal, the transpiration of the residual leaves is greatly weakened due to water deficit [11]. The leaf tissue is burned since there is not enough transpiration to remove the redundant heat. Furthermore, hydropenia and a high temperature accelerate the decomposition of pigments, resulting in the discoloration of damaged leaves [12]. Therefore, indicators that capture the canopy's greenness and humidity are usually used as features which characterize pest damage [13,14]. Additionally, defoliation is the most visible characterization of a host tree damaged by herbivorous insects and could be monitored using optical remote sensing data. However, optical remote sensing is only able to detect spectral changes in the canopy on a flat surface and fails to sense the vertical characteristics of damaged trees. Recently, increasing evidence has proved that the backscatter intensity of synthetic aperture radar (SAR) is sensitive to changes in both vegetation vertical structure and moisture [15,16], implying that SAR-derived features might be useful to monitor insect damage inducing the decay of the physiological vitality of the canopy. Therefore, many efforts have explored the applicability of the combination of optical and SAR data in mapping pest disturbances [14,17].

There are two approaches used to acquire the stress signal of a damaged canopy. The first involves detecting the remote sensing signal anomalies of the damaged canopy from single-time images during the pest infestation period. The second involves using signal variations in the damaged canopy between the pre- and post-disturbance periods. However, most studies assume that all physiological anomalies were caused by insect disturbances [8]. This assumption is sometimes questionable. Moso bamboo has typical phenological characteristics of on- and off-year periods within its growth cycle [18] (Figure 1). Specifically, after the unearthing of new bamboo shoots (approximately from April to May), the old leaves of maternal bamboo gradually yellow and shed from autumn. The new leaves sprout in the following spring and no bamboo shoots are produced that year. This is called the "off-year" period. The photosynthetic capacity of bamboo is greatly improved with the completion of new leaf expansion [19,20]. Bamboo begins to accumulate nutrients for shooting in the coming year. The period from the incubation to the produc-

tion of bamboo shoots is called "on-year". The morphology of off-year bamboo's canopy has many similarities (e.g., defoliation and discoloration) with on-year bamboo damaged by PPC. Previous studies have demonstrated that the physiological condition of off-year bamboo leaves has significant differences compared to normal on-year bamboo leaves, which can affect the identification accuracy of PPC damage [21]. Therefore, distinguishing off-year bamboo is essential for improving PPC damage detection using remote sensing. However, this hypothesis has not been tested.

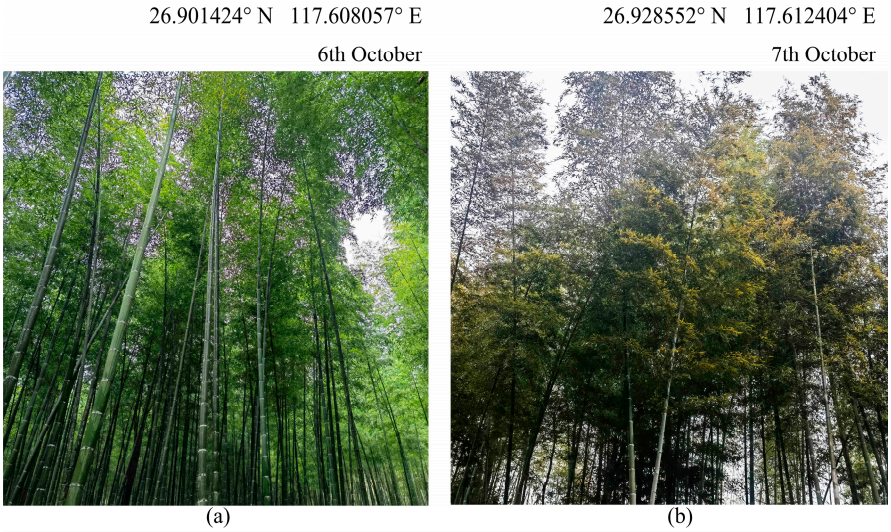

Figure 1. Comparison of (**a**) on-year and (**b**) off-year bamboo.

Accordingly, we attempted to map the distribution of PPC damage by the combined use of Sentinel-2 optical and Sentinel-1 SAR images. We investigated the ability of SAR and optical features to delineate PPC damage and assessed the impact of bamboo phenology on the mapping accuracy in respect of pest damage. Specifically, the following questions were investigated. (1) What are the responses of SAR and optical features to PPC damage? (2) What are the differences between the abilities of single-time and double-time observation features to identify PPC damage? (3) How is the identification accuracy of PPC damage affected by the on- and off-year phenological differences between bamboo forests?

2. Materials and Methods

2.1. Study Area

The study was conducted in Shunchang county, southeastern China (Figure 2). The forest coverage rate in the region was close to 80% in 2019. Moso bamboo, broadleaf (e.g., *Phoebe zhennan*, *Liquidambar formosana*), and coniferous (e.g., *Cunninghamia lanceolata*, *Pinus massoniana*) forests are the main forest types in the region. Shunchang county is also known as one of the "bamboo townships" of China. Various bamboo insect disturbance events occur here every year. Although the local forestry bureau and foresters have made enormous efforts in respect of pest control, bamboo pests, especially PPC, still present intermittent outbreaks.

2.2. Data Used

2.2.1. Field Observations

Field observations were conducted from 28 September to 15 October 2020. We randomly selected observation plots (15 × 15 m) in the bamboo forest area. The central point coordinate of each plot was recorded using a handheld global positioning system instrument (GPS, UniStrong G120BD). Two technicians visually estimated the defoliation rate (the percentage of leaf loss in the crown) of each Moso bamboo plant within the plot. The defoliation rate of each plot was calculated as the average of estimates by two technicians and was used to determine the damage severity (0–10% denoted healthy, 11–25% denoted mild

damage, 26–50% denoted moderate damage, and >51% denoted severe damage). In total, 267 bamboo plots were observed, including 126 on-year and 141 off-year bamboo plots. The 126 on-year plots consisted of 19 severely damaged plots, 18 moderately damaged plots, 40 mildly damaged plots, and 49 healthy plots. The 141 off-year bamboo plots comprised 21 severely damaged plots, 22 moderately damaged plots, 53 mildly damaged plots, and 45 healthy plots. In addition, we sampled 27 broadleaf plots and 31 coniferous plots.

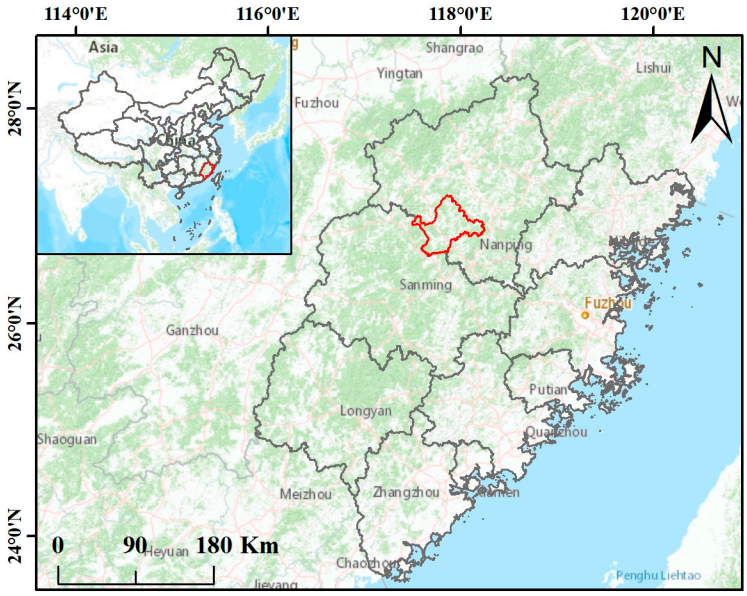

Figure 2. Location of Shunchang County, Nanping City, Fujian Province, China.

2.2.2. Remote Sensing Data Used

A total of 15 images, including 6 Sentinel-1 Level-1 Ground Range Detected products and 9 cloudless Sentinel-2 Level-1C products, were downloaded from the Copernicus Open Access Hub (Table 1).

Table 1. Remote sensing imagery used for PPC damage monitoring.

Sensors	Observation Time	Tile/Absolute Orbit Numbers
Sentinel-2	21 February 2020 16 April 2020 23 October 2020	T50RNQ, T50RNR, T50RPQ
Sentinel-1	22 February 2020 22 April 2020 19 October 2020	031, 364 032, 239 034, 864

Sentinel-1 images were pre-processed on the Sentinel Application Platform v7.0 of the European Space Agency (ESA). The thermal noise of the images was removed to enhance the continuities of sub-swaths. The backscattered signals at vertical–horizontal (VH) and vertical–vertical (VV) polarizations were converted into radar cross-sections (σ^o) through radiometric correction. The speckle of the corrected images was reduced using the refined Lee filter (window size: 7 × 7 pixels). The geometric distortion of the images was corrected using the range Doppler terrain correction method. The spatial resolution of the images was resampled to 10 m during this step. Finally, logarithmic transformation was performed to covert the unitless backscatter coefficient into decibels (dB) [22].

The Sen2Cor plugin provided by the ESA was used to conduct the atmospheric correction of Sentinel-2 images. All bands were resampled into 10 m using the Sen2Res plugin [23]. The topographic correction of the Sentinel-2 images was implemented with the SCS + C model and digital elevation model (DEM) data, which were resampled from

12.5 m DEM data (ALOS-1) acquired from NASA (https://earthdata.nasa.gov) using the nearest-neighbor method.

According to the observation time for collected data, the pre-processed images were categorized into three classes and abbreviated as $SC2020_{Feb}$ (images from February), $SC2020_{Apr}$ (images from April), and $SC2020_{Oct}$ (images from October) for facilitating description. Additionally, polygons with 2 × 2 pixels centered on the GPS observation of each plot were sketched to retrieve data used to construct the models.

2.3. Mapping the Distribution of Bamboo Forests

With Google Earth images, local forestry inventory data, and the coordinates collected from the field investigation, polygons for different forest types (coniferous, broadleaf, on-year bamboo, off-year bamboo) were sketched for training the model. The normalized difference moisture index (NDMI), bamboo index (BI), and normalized difference vegetation index red-edge ($NDVI_{re}$) were calculated for mapping bamboo distribution [24,25]. Extreme gradient boosting (i.e., XGBoost, see Section 2.5.1 for detailed description) was applied to generate the distribution map of bamboo forests (Figure A1). Assessed using collected samples, the classification accuracy reached 90.88% (Table A1).

2.4. Feature Selection

Previous studies have demonstrated that PPC infestation induces detectable declines in the chlorophyll, moisture, and nitrogen contents of host leaves [21]. Therefore, 35 spectral indices [14,26–28] and 5 SAR indicators [15,29,30] that have been demonstrated to be tightly linked with pigment contents, humidity, and canopy structure were calculated as candidates for further analysis (Table A2). All variables were uniformly normalized between 0 and 1.

The recursive feature elimination (RFE) method was applied to select features sensitive to PPC damage [31]. RFE is a greedy optimization algorithm. Its principle is to eliminate features, making a poor contribution to the model through iteration according to the performance of each variable in the classification process. XGBoost was applied as the base evaluator of RFE. After traversing the variable space, the variable subset that contributed the most to the classification results was selected as the input features for model construction.

2.5. Development of Severity Identification Model

2.5.1. Model Establishment and Optimization

The PPC damage identification model was constructed using XGBoost, which is one of the most representative ensemble algorithms of machine learning [32]. The principle of XGBoost is to accumulate multiple base learners (e.g., decision trees) and form a strong classifier through iteration. Several studies have demonstrated that XGBoost performs better than the random forest model after appropriate hyper-parameter adjustment [33,34].

There are 5 main parameters in XGBoost: ① the boosting learning rate (LR), ② the number of the base learner (NE), ③ the maximum tree depth of the base learner (MD), ④ the minimum sum of the instance weight needed in a child (MCW), and ⑤ the minimum value of the loss function required for leaf node branching (GAM). Each hyper-parameter was calibrated using the grid search method in conjunction with 10-fold cross-validation.

2.5.2. Design of Model Scenario

To evaluate the importance of differentiating between bamboo phenologies in the identification of PPC damage, models were established using total samples, on-year samples, and off-year samples. We also compared the applicability of single-time and double-time observation features in monitoring PPC damage. According to the PPC damage period and field campaign time, single-time observation features were generated using $SC2020_{Oct}$. Double-time observation features were calculated according to the differences in remote sensing signals between post- (i.e., $SC2020_{Oct}$) and pre-disturbance periods (i.e., $SC2020_{Feb}$ or $SC2020_{Apr}$). Finally, a total of 9 scenarios were designed and evaluated (Table 2).

Table 2. The designed experimental scenarios.

Scenario	Model Input	Model Abbreviation
Single-time observation (October)	On-year samples	Single-on
	Off-year samples	Single-off
	Total	Single-BF
Double-time observation (October–February)	On-year samples	Double-on$_{Feb}$
	Off-year samples	Double-off$_{Feb}$
	Total	Double-BF$_{Feb}$
Double-time observation (October–April)	On-year samples	Double-on$_{Apr}$
	Off-year samples	Double-off$_{Apr}$
	Total	Double-BF$_{Apr}$

2.5.3. Accuracy Evaluation

A total of 70% of the sample data (training set) were randomly selected for training the model and the remaining 30% of sample data (test set) were used for validating the model performance. The sample size of each severity group varied greatly, which could have caused over-fitting problems during the model training process. To tackle this issue, the sample data were pre-processed using the synthetic minority over-sampling technique [35]. Its principle is to oversample (i.e., random linear interpolation) the minority class by using KNN (k-nearest neighbor), thus balancing the sample size of each class group.

In the training process, after the optimization of the hyper-parameters of each model, its training effect was assessed using 10-fold cross-validation. The model generality was further evaluated using the test set. The model performance was assessed by overall accuracy (OA), user accuracy (UA), and producer accuracy (PA).

3. Results

3.1. Optical and SAR Signals of Bamboo Forests with Different Damage Severities

The statistics of the spectrum and two SAR signals of samples in each damaged group were calculated (Figure 3). The spectrum of damaged samples presented high reflectivity in the visible region compared with healthy samples. With the increase in the PPC attack, the canopy reflectance decreased in the red-edge region, and its magnitude varied more visibly in longer wavelengths, i.e., red-edge$_{740}$ and red-edge$_{783}$. The spectral differences among damaged groups were most evident in the near-infrared region. The reflectance dropped notably in this wavelength with the increase in damage severity. The reflectance in the shortwave infrared wavelength is normally linked with the moisture content of the canopy, i.e., a higher moisture content leads to a lower reflectance in this region and vice versa. However, the observational data showed that there was no distinct spectrum variation in damaged samples in the two shortwave infrared bands. On- and off-year samples exhibited a visible spectral difference in each damaged group. The reflectance of off-year samples was relatively lower than that of on-year samples, except for the moderately damaged group.

As for the backscatter signals (not normalized) of each damaged group, the $\sigma^o vv$ and $\sigma^o vh$ of bamboo forests decreased noticeably at the initial stage of PPC damage, especially for the on-year samples. However, the signals had no visible changes when the damage severity was further increased. It is noteworthy that the $\sigma^o vv$ and $\sigma^o vh$ values of damaged off-year samples were higher than those of on-year samples, which differed from the changing pattern of the spectrum.

3.2. Model Performance

3.2.1. Classification Results

The features that contributed the most to the performance improvement of each model were selected based on RFE (Figure 4). Table 3 shows the determined hyper-parameter and OA values of the constructed models. The OA values of the training set (OA $\pm$ standard error) and test set confirm that there is no over-fitting problem in each model.

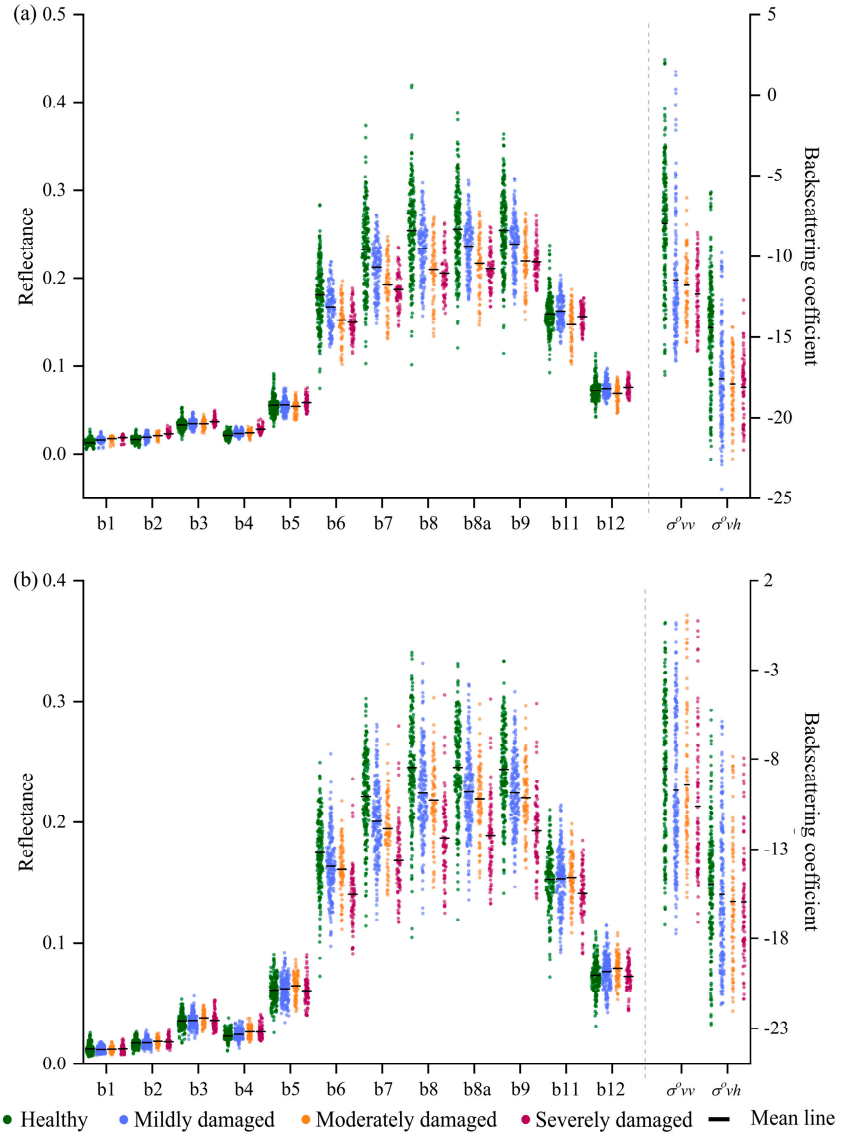

Figure 3. The spectra and SAR signals of (**a**) on-year and (**b**) off-year bamboo forests with different damage severities. b1~b9 represent the coastal, blue, green, red, red-edge$_{705}$, red-edge$_{740}$, red-edge$_{783}$, NIR, NIR$_{narrow}$, and water vapor bands of Sentinel-2 imagery, while b11~b12 represent the SWIR-1 and SWIR-2 bands of Sentinel-2 imagery.

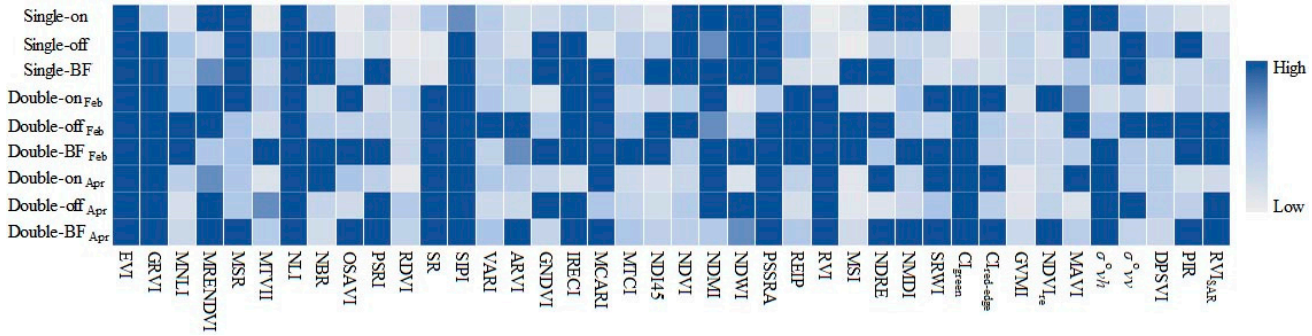

Figure 4. The contribution ranking of different features in each model.

Table 3. The determined hyper-parameters and classification accuracies of each model.

Model	Hyper-Parameters					OA (%)	
	LR	NE	MD	MCW	GAM	Training Set	Test Set
Single-on	0.32	73	6	1	0	89.29 ± 1.05	88.00
Single-off	0.28	62	6	1	0.3	88.65 ± 1.15	85.80
Single-BF	0.3	183	6	1	0	85.24 ± 1.30	82.76
Double-on$_{Feb}$	0.3	109	6	2	0	87.22 ± 1.24	84.67
Double-off$_{Feb}$	0.3	61	6	1	0	80.72 ± 1.97	75.15
Double-BF$_{Feb}$	0.25	207	6	1	0	81.59 ± 1.46	78.06
Double-on$_{Apr}$	0.3	172	6	1	0	86.90 ± 1.09	83.33
Double-off$_{Apr}$	0.32	89	6	1	0	78.36 ± 1.28	76.92
Double-BF$_{Apr}$	0.15	101	6	1	0	79.08 ± 0.72	75.24

Figure 5 shows the outputs for the test set samples. For on-year samples, the Single-on model outperformed double-time observation feature-based models, with OA values higher by at least 3%. The models all had great ability to distinguish healthy, moderately damaged, and severely damaged samples; however, the Double-on$_{Feb}$ and Double-on$_{Apr}$ models performed relatively poorly in identifying mildly damaged samples, i.e., their PA and UA values were below 80%. For off-year samples, the Single-off model performed better than the double-time observation feature-based models, with an OA value higher by about 10%. The PA and UA values of the Single-off model were about 90% for healthy and severely damaged samples. The PA and UA values for mildly damaged samples were 82.76% and 84.21%, respectively. However, this model performed relatively poorly for moderately damaged samples. When on- and off-year samples were combined, the performances of the double-time observation feature-based models were poorer than that of the Single-BF model, owing to their failure to properly identify damaged off-year samples.

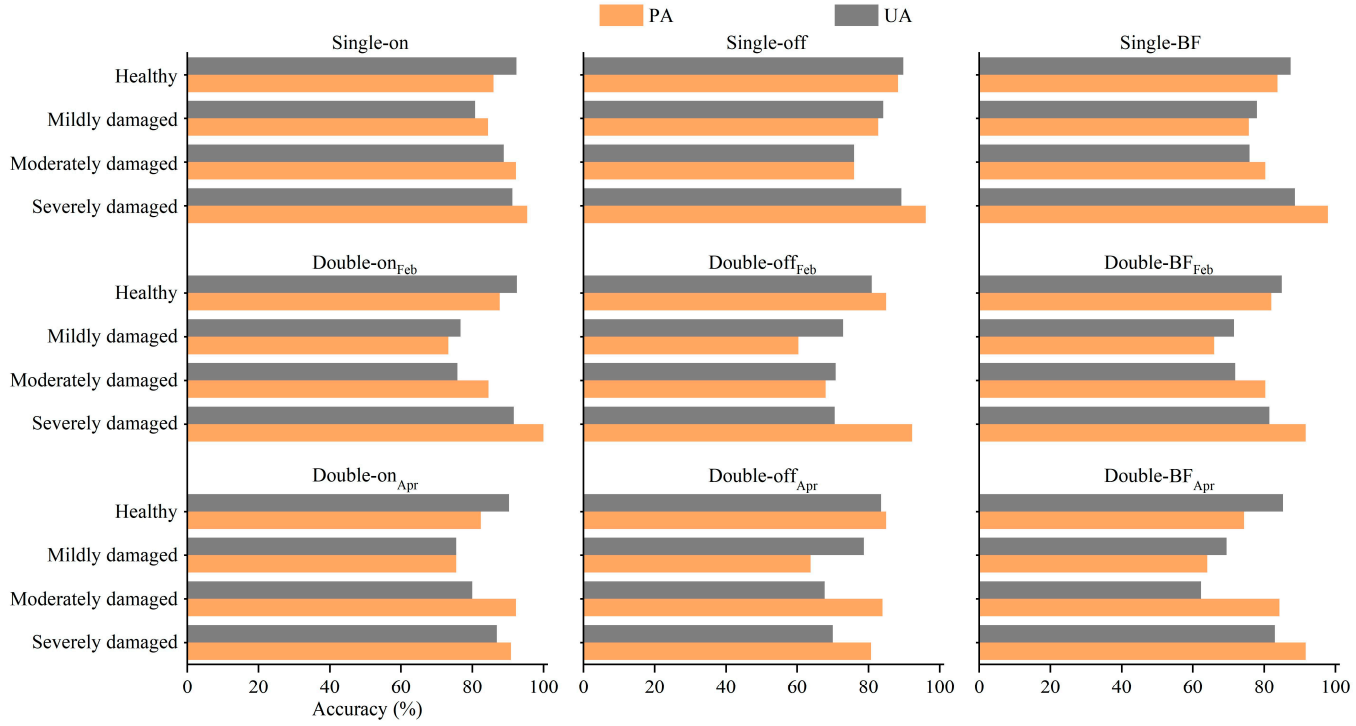

Figure 5. The performance (PA and GA) of each model in different damage groups.

The performances of Single-on + Single-off (the Single-on and Single-off models were used for on- and off-year samples, respectively) and Single-BF were further compared (Figure 6). The OA value of the former was 4% higher than that of the latter. The accuracy

of Single-on + Single-off in all damaged groups was higher than that of Single-BF, except for the severely damaged group. Specifically, 16.24% of healthy samples were wrongly classified into the mildly damaged group by Single-BF. The misclassification rate for the mildly damaged group was the highest, with 12.62% and 11.65% of this group's samples being misclassified into the healthy group and moderately damaged group, respectively. A total of 11.76% of moderately damaged samples were misclassified into the severely damaged group. This comparison indicates the importance of differentiating between on- and off-year samples for detecting different degrees of PPC damage.

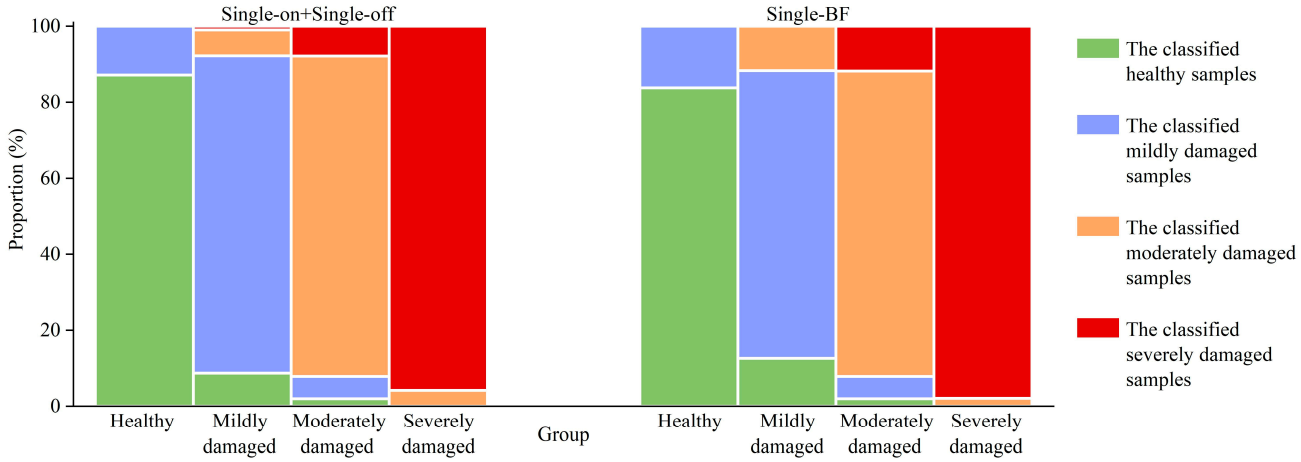

Figure 6. Comparison of Single-on + Single-off and Single-BF models in identifying samples of different damage severities.

3.2.2. Contribution of SAR Features to Classification Model

To evaluate the contribution of SAR features to PPC damage identification, the responses of selected features in the Single-on and Single-off models to pest infestation were analyzed. We trained the model only based on optical features (model$_{spec}$, Table A3) to quantitatively evaluate the role of SAR features in identifying PPC damage by comparing its performance with that of optical and SAR feature-based models (i.e., Single-on and Single-off).

Compared with the healthy samples, the optical features of damaged samples generally exhibited upward or downward trends, and the variation magnitudes increased with the increase in damage severity (Figure 7). In comparison, the values of SAR features (i.e., $\sigma^o vh$ in Single-on; $\sigma^o vv$ and PIR in Single-off) were relatively discrete. The one-way ANOVA method was used to assess the ability of SAR features to discriminate PPC damage severity. The p-value of the one-way ANOVA indicates the significance of differences between different health level groups. As shown in Table 4, the differences in SAR features between various damage groups were not always statistically significant. The differences between mildly and moderately, mildly and severely, and moderately and severely damaged samples were insignificant.

The performance of model$_{spec}$ was generally poorer than that of the optical and SAR feature-based model (Figure 8). For on-year samples, in comparison with the Single-on model, the Single-on$_{spec}$ model had slightly higher OA for the training set, but a 1.33% lower OA for the test set. The role of SAR features in distinguishing damaged off-year samples was more evident. The OA values of Single-off were 3.70% and 2.37% higher than those of Single-off$_{spec}$ for the training and test sets, respectively. SAR features were mainly useful for identifying the healthy and mildly damaged samples, especially the latter. For the mildly damaged samples, the PA and UA of Single-on were 4.44% and 0.85% higher than those of Single-on$_{spec}$, respectively. The PA and UA of Single-off were 6.90% and 2.73% higher than those of Single-off$_{spec}$, respectively.

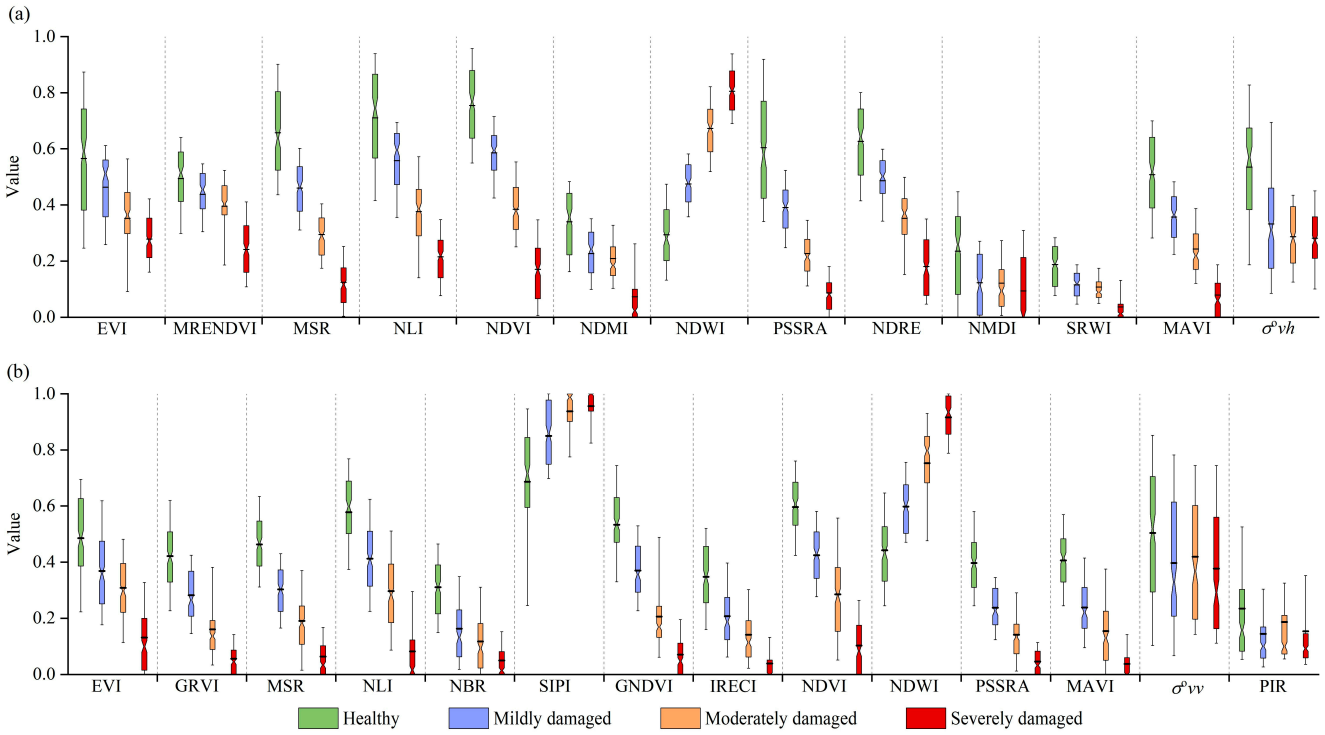

Figure 7. Features values of (**a**) Single-on and (**b**) Single-off in different pest severity groups.

Table 4. Differences in SAR features among different severity groups.

Compared Groups	$\sigma^o vh$/Single-On	$\Sigma^o vv$/Single-Off	PIR/Single-Off
Healthy–Mildly damaged	0.000 **	0.000 **	0.001 **
Healthy–Moderately damaged	0.000 **	0.003 **	0.302
Healthy–Severely damaged	0.000 **	0.000 **	0.007 **
Mildly damaged–Moderately damaged	0.121	0.429	0.242
Mildly damaged–Severely damaged	0.054	0.492	0.998
Moderately damaged–Severely damaged	0.999	0.120	0.648

Note: ** denote the significance at levels of 0.01.

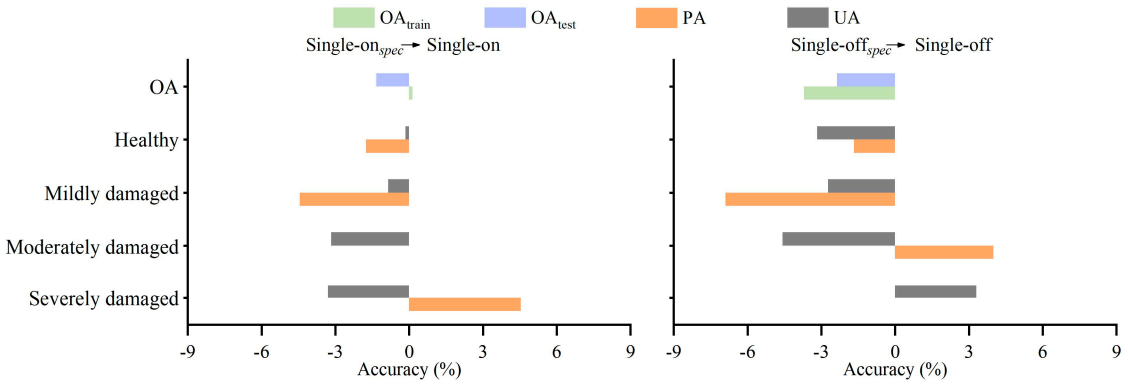

Figure 8. Differences in the performance of models constructed using optical features and optical and SAR features. Values shown are the PA and UA of the optical model minus those of the optical and SAR features model.

3.3. Distribution of PPC Damage

A distribution map of PPC damage was generated using the best Single-on and Single-off models, and the area proportions of bamboo in various damage severity groups were counted (Figure 9). In the study area, 53.05% of bamboo forests were damaged by PPC at

different severities. The area proportions of bamboo forests with severe, moderate, and mild PPC damage severities were 16.83%, 14.07%, and 22.15%, respectively. The area proportion of off-year bamboo damaged by PPC was 55.77% higher than the corresponding value for on-year bamboo (51.25%). Severely damaged areas accounted for 24.12% of off-year and 12.01% of on-year bamboo forests.

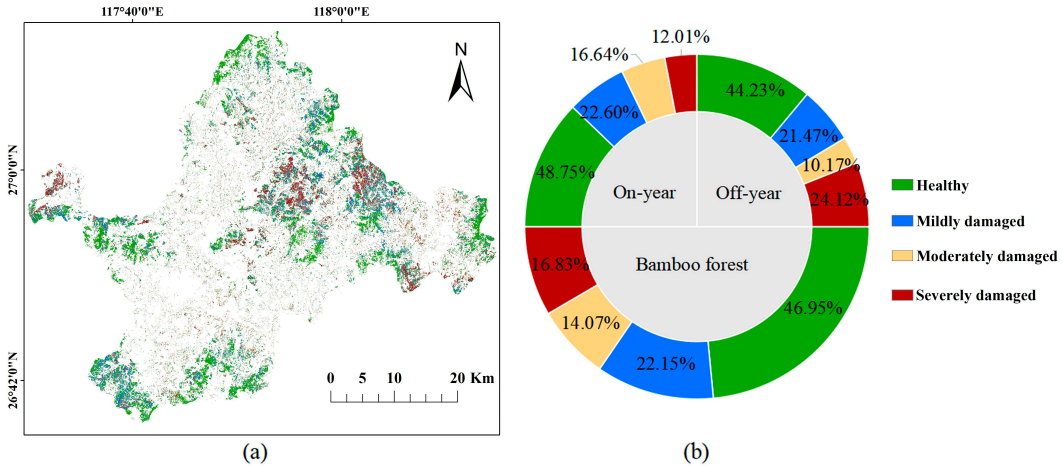

Figure 9. (**a**) Spatial distribution of PPC damage severity and (**b**) area proportions of different severity groups in the study area.

The impact of topographic conditions on PPC infestation was further analyzed (Figure 10). As for on-year bamboo forests, the occurrence of pest damage had evident vertical differences. PPC damage occurred mainly in lower-altitude areas, and the severity changed inversely with elevation. In contrast, the effect of elevation on PPC damage was not visible for off-year bamboo forests. The moderate and severe PPC damage mainly occurred in areas with slopes ranging from 15° to 20° for on-year bamboo forests and ranging from 20° to 25° for off-year forests. Mildly damaged bamboo forests were concentrated in the northeast area, while the moderately and severely damaged areas were mostly located on the shady slope, i.e., the north side.

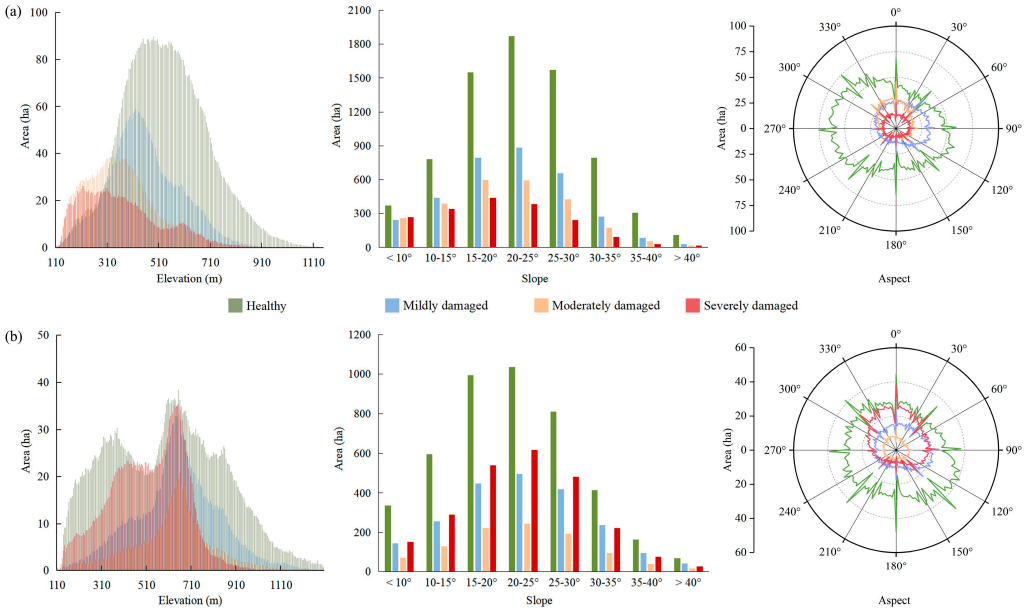

Figure 10. Changes in areas of different PPC damage severities with terrain conditions in (**a**) on-year bamboo forest and (**b**) off-year bamboo forest.

4. Discussion

4.1. Significance of SAR Features to PPC Monitoring

The correlation between backscattering signals and the physiological characteristics of vegetation implies the application potential of SAR in monitoring insect disturbance [15,16]. However, SAR is extremely sensitive to topographic conditions. Its active remote mode for side imaging will cause distortion of backscattering signals over complex terrain areas, which increases the uncertainty of interpretation results [36]. According to the values of selected features, the SAR features were more discrete than the optical features, and their ability to differentiate between the severities of damaged samples was weak. Therefore, SAR (at least C-band SAR) cannot be independently used to monitor PPC damage. Although the results indicate the priority of optical features over SAR, this does not imply that SAR provides no useful information for pest damage identification. The sensitivity of electromagnetic waves to the dielectric constant and geometric structure of the objective means that SAR can capture information with regards to canopy defoliation and moisture decline caused by PPC. The improved performance of the model combining optical and SAR features confirms the contribution of SAR in identifying healthy and damaged bamboo forests.

4.2. Interference Factors during the PPC Damage Identification

For the study area, the imaging time of cloudless optical satellite data is mostly at the beginning or end of a year. On- and off-year bamboo forests show great characterization differences during these periods. Off-year bamboo has lower leaf chlorophyll and moisture contents than on-year bamboo [21]; its canopy spectrum is similar to damaged or more severely damaged on-year bamboos.

The different management of on- and off-year bamboo forests will also affect their remote sensing signals. To ensure the shoot yield in the coming year, farmers will spray pesticides once or twice a year in on-year bamboo forests. The first pest prevention procedure is conducted during the overwintering-generation of PPC, i.e., approximately in March–April. The second control procedure is normally conducted in the summer, varying with the degree of the first-generation larvae threatening the bamboo forests. Conversely, there is usually no manual pest prevention or control procedure in the off-year bamboo forests since they do not yield shoots in the following year. Therefore, the area proportion of PPC damage in the off-year bamboo is notably higher relative to that of the on-year bamboo. Additionally, farmers normally carry out understory weeding of on-year bamboo in autumn and winter to facilitate shoot harvesting in the coming year, while there is no weeding in the off-year region (Figure 11). The observed proportion of bamboo forest background will increase when the defoliation rate rises, which has a particularly noticeable impact on SAR. Healthy off-year bamboo forests have lower backscattering coefficients than on-year forests. The backscattering coefficient in damaged areas is higher than that of on-year bamboo forests, owing to the compensation of the bamboo forest's background.

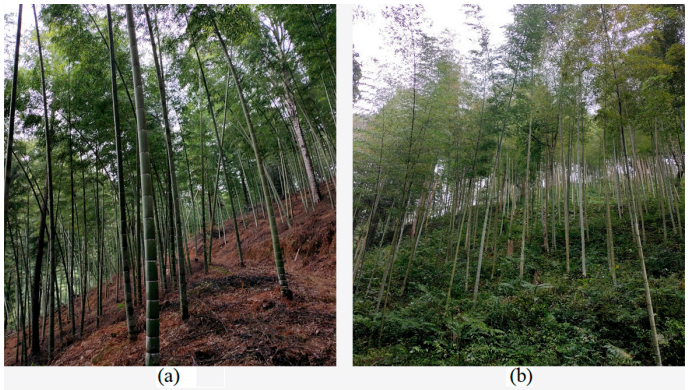

Figure 11. Understory vegetation of (**a**) on-year bamboo forests and (**b**) off-year bamboo forests.

There are notable differences in canopy characteristics and understory vegetation conditions between on- and off-year bamboo forests. Remote sensing signals for healthy off-year samples are close to those of damaged on-year samples, which will affect the accuracy of PPC damage classification. When the on- and off-year samples are combined, the damaged area will be underestimated in on-year bamboo forests and overestimated in off-year regions (Figure 12).

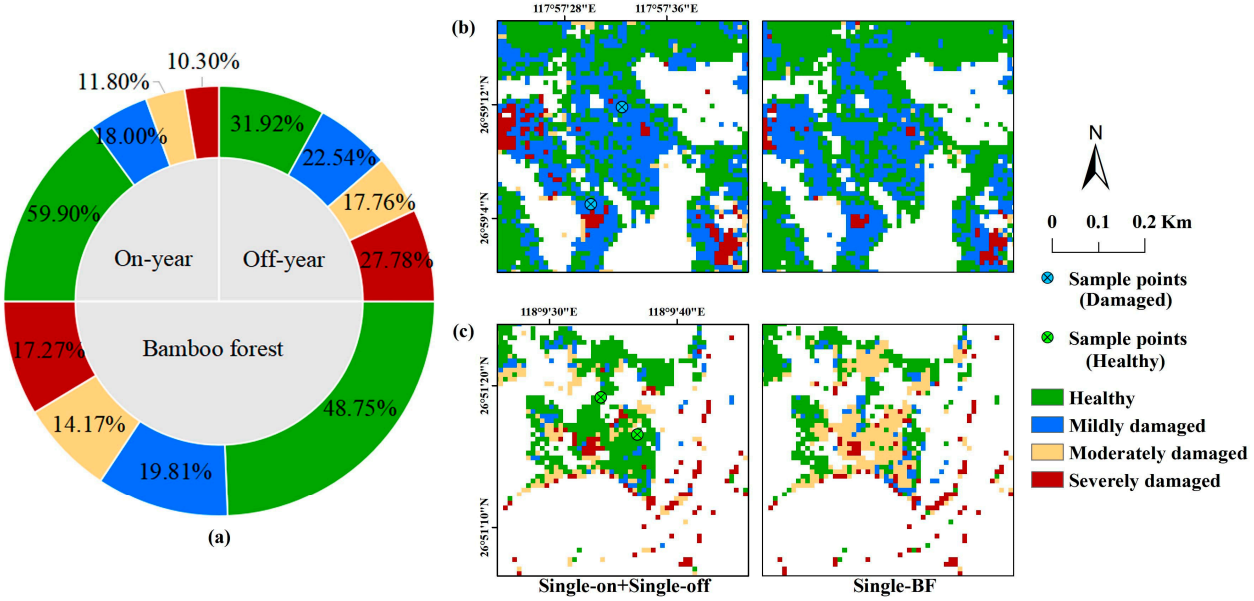

Figure 12. (**a**) The area proportions of bamboo forests with different damage severities output by Single-BF. A comparison of Single-on + Single-off and Single-BF in (**b**) on-year and (**c**) off-year areas.

Pests are not the only disturbance factors in forest ecosystems [8]. As fast-growing economic forests, the magnitude and frequency of selective logging events in bamboo forests are intensive every year. Generally, to maximize the management benefits of bamboo forests, the logging events are mostly conducted in the off-year areas [36,37]. However, the price of bamboo products is the main driver affecting the logging enthusiasm of farmers. Logging events will also be conducted in on-year bamboo forests when the price of bamboo products is attractive. Logging events will drastically change the characteristics (e.g., reflectance and structure) of the canopies of bamboo forests, which could cause the overestimation of areas damaged by PPC (Figure 13). This is the reason why the double-time observation feature-based model performed poorly in identifying PPC damage, especially for the off-year bamboo forests.

Compared with the Single-on + Single-off model, the double-time observation feature-based model outputs a lower severely damaged area and a higher mildly damaged area. This may be caused by overwintering-generation pest damage and spatial heterogeneity in the leaf change rate. For instance, the nutrient contents of on-year bamboo leaves were at a low status early in the year. By October, the bamboo leaves had matured. However, the pest damage reduced the nutrient content of bamboo leaves. Therefore, the physiological difference in the damaged area between October and the pre-disturbance period of PPC was theoretically smaller than in the healthy area. It is noteworthy that the overwintering-generation larvae are active in April; thus, many forestry areas have been attacked. The vitality of the damaged canopy will be recovered when the overwintering-generation larvae are cocooned. However, if the area is attacked by PPC again, the difference in remote sensing signals from those in April will be greater than those in the area that is not damaged by the overwintering generation of PPC. In February, Moso bamboo has not yet completed leaf changing [38]. Since the climate and stand conditions change with elevation and latitudes, the leaf changing rates of the bamboo forests are spatially heterogeneous,

inducing uncertainty in PPC damage detection. Therefore, for Moso bamboo forests with intensive disturbance frequency, the single-time observation feature-based model is the optimal choice for PPC monitoring.

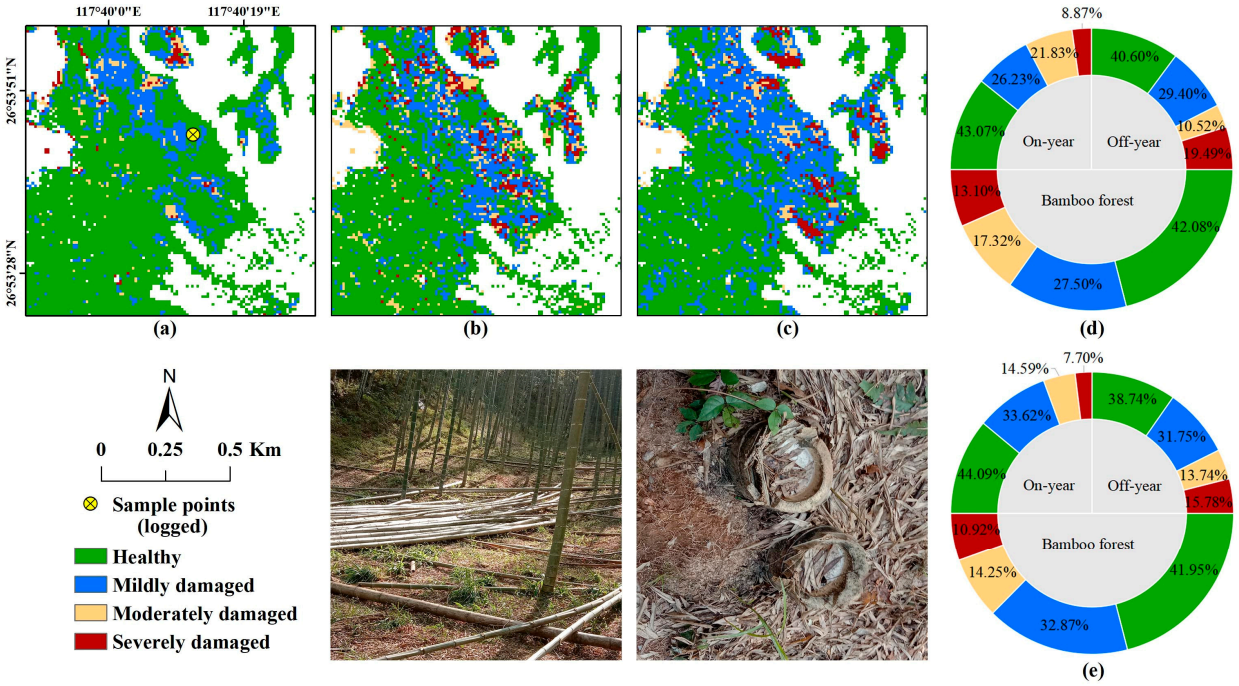

Figure 13. Distribution of PPC damage detected using (**a**) Single-on + Single-off, (**b**) Double-on$_{Feb}$ + Double-off$_{Feb}$, and (**c**) Double-on$_{Apr}$ + Double-off$_{Apr}$ in a typical area (selectively logged). The area proportions of bamboo forests with different damage severities output by (**d**) Double-on$_{Feb}$ + Double-off$_{Feb}$ and (**e**) Double-on$_{Apr}$ + Double-off$_{Apr}$.

4.3. Limitations and Research Prospects

Summer is theoretically the key period for PPC damage identification, since the first-generation larvae of PPC pose the greatest threat to bamboo forests. However, the deficiencies in spaceborne optical images for this period constrain the construction of pest-monitoring models. Additionally, the management pattern of bamboo forests varies spatially. Farmers who adopt extensive management rarely weed the understory vegetation of on-year bamboo forests, while manual intervention in intensive management areas is more regular. Therefore, under the same damage severity of PPC, remote sensing signals in extensive and intensive regions might exhibit a great difference.

The unmanned aerial vehicle (UAV) technique provides a novel and flexible selection for monitoring forestry insect disturbance [39,40]. Hyperspectral and light detection and ranging (LIDAR) data at spatial resolutions of several centimeters acquired by UAV can be used to detect subtle structural and spectral changes in the host's canopy and to eliminate the interference from logging and background, which is valuable for the selection of various disturbance endmembers, the development of methods detecting PPC damage, and the validation of damage severity detected using satellite data. The combined application of satellite and UAV data in PPC damage detection is worthy of investigation.

5. Conclusions

We combined Sentinel-1 and Sentinel-2 data to monitor PPC damage at a 10 m resolution. It was found that bamboo phenology (i.e., on- and off-year) can notably affect PPC damage identification. With the differentiation between on-year and off-year bamboo, the OA value was improved by 4%. The single-time observation feature-based model was more suitable for PPC monitoring than the double-time observation feature-based model. Its OA values were at least 3% and 10% higher than the latter for on- and off-year samples,

respectively. Manual interference (e.g., logging and weeding) was the main reason for the poor performance of the double-time observation feature-based model. The selected optical and SAR features exhibited different responses to PPC damage, of which the optical features presented regular reduction or increasing trends with the increase in damage severity. SAR data alone were not suitable for identifying different degrees of damage severity. The difference in SAR signals between healthy and damaged samples was significant. The addition of SAR data to optical features could improve the model performance, mainly for healthy and mildly damaged samples.

Author Contributions: Conceptualization, X.H., W.J. and Z.X.; methodology and software, X.H.; data collection and process, X.H., Q.Z., L.H. and T.Z.; validation, X.Z. and Y.Z.; writing—original draft preparation, X.H.; writing—review and editing, W.J.; project administration, W.J. and Z.X.; funding acquisition, W.J. and Z.X. All authors have read and agreed to the published version of the manuscript.

Funding: This research was funded by the National Key R&D Program of China, grant number 2019YFA0606601; the National Natural Science Foundation of China, grant number 42071300; the China Postdoctoral Science Foundation, grant number 2018M630728; and the Fujian Province Natural Science Foundation Project, grant number 2020J01504.

Data Availability Statement: Not applicable.

Acknowledgments: We are grateful to the Forestry Bureau of Shunchang County for their help in this work. Special thanks to Juyuan Gao for his help in the field experiment of this research. Comments made by the anonymous reviewers are greatly appreciated.

Conflicts of Interest: The authors declare no conflict of interest.

Appendix A

Table A1. Confusion matrix for bamboo forest extraction results.

	Coniferous	Broadleaf	Off-Year Bamboo	On-Year Bamboo	PA (%)	UA (%)	OA (%)
Coniferous	191	28	2	2	85.65	90.09	90.88
Broadleaf	17	187	5	5	87.38	85.39	
Off-year bamboo	4	1	203	10	93.12	95.31	
On-year bamboo	0	3	3	216	97.30	92.70	

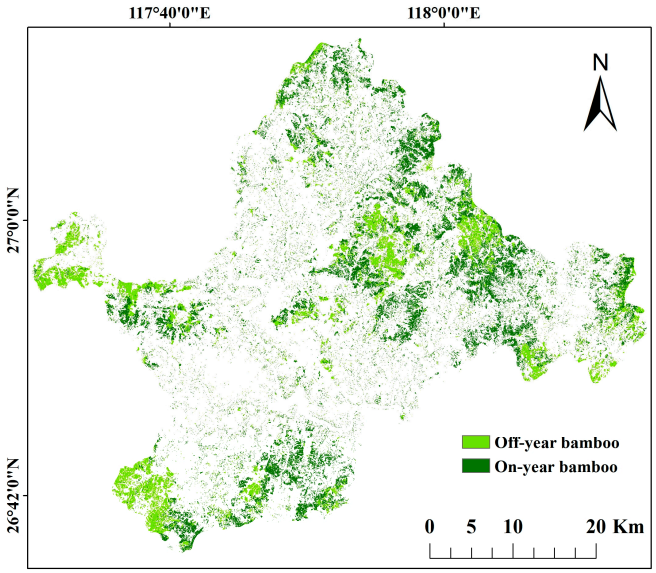

Figure A1. Distribution of extracted bamboo forests.

Table A2. Candidate variables used for PPC damage identification.

Index	Formula
Enhanced Vegetation Index	$EVI = \frac{2.5\times(b8-b4)}{b8+6\times b4-7.5\times b2+1}$
Green Ratio Vegetation Index	$GRVI = b8/b3$
Modified Non-Linear Index	$MNLI = \frac{(b8^2-b4)\times 1.5}{b8^2+b4+0.5}$
Modified Red-Edge Normalized Difference Vegetation Index	$MRENDVI = \frac{b6-b5}{b6+b5-2\times b1}$
Modified Simple Ratio	$MSR = \frac{b8/b4-1}{\sqrt{b8/b4+1}}$
Modified Triangular Vegetation Index (Improved)	$MTVII = \frac{1.5\times[1.2\times(b6-b3)-2.5\times(b4-b3)]}{\sqrt{(2\times b6+1)^2-(6\times b6-5\times\sqrt{b4})-0.5}}$
Non-Linear Index	$NLI = \frac{b8^2-b4}{b8^2+b4}$
Normalized Burn Ratio	$NBR = \frac{b8-b12}{b8+b12}$
Optimized Soil-Adjusted Vegetation Index	$OSAVI = \frac{1.5\times(b8-b4)}{b8+b4+0.16}$
Plant Senescence Reflectance Index	$PSRI = (b4-b2)/b6$
Renormalized Difference Vegetation Index	$RDVI = \frac{b8-b4}{\sqrt{b8+b4}}$
Simple Ratio	$SR = b8a/b4$
Structure Insensitive Pigment Index	$SIPI = \frac{b7-b1}{b7-b4}$
Visible Atmospherically Resistant Index	$VARI = \frac{b3-b4}{b3+b4-b2}$
Atmospherically Resistant Vegetation Index	$ARVI = \frac{b8-(2\times b4-b2)}{b8+(2\times b4-b2)}$
Green Normalized Difference Vegetation	$GNDVI = \frac{b7-b3}{b7+b3}$
Inverted Red-Edge Chlorophyll Index	$IRECI = \frac{b7-b4}{b5/b6}$
Modified Chlorophyll Absorption Ratio Index	$MCARI = [(b5-b4)-0.2\times(b5-b3)]\times(b5/b4)$
Meris Terrestrial Chlorophyll Index	$MTCI = \frac{b6-b5}{b5-b4}$
Normalized Difference Index	$NDI45 = \frac{b5-b4}{b5+b4}$
Normalized Difference Vegetation Index	$NDVI = \frac{b8-b4}{b8+b4}$
Normalized Difference Moisture Index	$NDMI = \frac{b8a-b12}{b8a+b12}$
Normalized Difference Water Index	$NDWI = \frac{b3-b8}{b3+b8}$
Pigment Specific Simple Ratio algorithm	$PSSRA = b7/b4$
Red-Edge Inflection Point Index	$REIP = 705+\frac{35\times[(b4+b7)/2-b5]}{b6-b5}$
Ratio Vegetation Index	$RVI = b8/b4$
Moisture Stress Index	$MSI = b12/b8$
Normalized Difference Red-Edge	$NDRE = \frac{b6-b5}{b6+b5}$
Normalized Multi-band Drought Index	$NMDI = \frac{b8a-(b11-b12)}{b8a-(b11+b12)}$
Simple Ratio Water Index	$SRWI = b12/b8a$
Green Chlorophyll Index	$CI_{green} = b7/b3-1$
Red-Edge Chlorophyll Index	$CI_{red-edge} = b7/b5-1$
Global Vegetation Moisture Index	$GVMI = \frac{(b8+0.1)-(b12+0.02)}{(b8+0.1)+(b12+0.02)}$
Normalized Difference Vegetation Index Red-Edge	$NDVI_{re} = \frac{b8-b5}{b8+b5}$
Moisture Adjusted Vegetation Index	$MAVI = \frac{b8-b4}{b8+b4+b12}$
Dual Polarization SAR Vegetation Index	$DPSVI = \frac{(\sigma^o vv_{max}-\sigma^o vv)+\sigma^o vh}{\sqrt{2}}\times\frac{\sigma^o vv+\sigma^o vh}{\sigma^o vv}\times\sigma^o vh$
Polarization Intensity Ratio	$PIR = \sigma^o vh/\sigma^o vv$
Radar Vegetation Index	$RVI_{SAR} = \frac{4\times\sigma^o vh}{\sigma^o vv+\sigma^o vh}$
Backscattering at Cross-polarization (VH) and Co-polarization (VV)	$\sigma^o vh$, $\sigma^o vv$

Note: b1~b8a and b11~b12 represent the coastal, blue, green, red, red-edge$_{705}$, red-edge$_{740}$, red-edge$_{783}$, NIR, NIR$_{narrow}$, SWIR-1 and SWIR-2 bands of Sentinel-2 imagery.

Table A3. Constructed models that are only based on spectral features.

Model	Hyper-Parameters					Features
	LR	NE	MD	MCW	GAM	
Single-on$_{Spec}$	0.24	83	6	1	0	EVI, MRENDVI, MSR, NLI, NDVI, NDMI, NDWI, PSSRA, NDRE, NMDI, SRWI, MAVI
Single-off$_{Spec}$	0.35	70	6	1	0	GRVI, NLI, NBR, SIPI, GNDVI, IRECI, NDVI, NDMI, NDWI, PSSRA, NDRE, GVMI, MAVI

References

1. FAO. *Global Forest Resources Asessment 2020: Main Report*; Food and Agriculture Organization of the United Nations: Rome, Italy, 2020.
2. National Forestry and Grassland Administration. *China Forest Resources Report (2014–2018)*; China Forestry Publishing House: Beijing, China, 2019.
3. Cao, L.; Coops, N.C.; Sun, Y.; Ruan, H.H.; Wang, G.B.; Dai, J.S.; She, G.H. Estimating canopy structure and biomass in bamboo forests using airborne LiDAR data. *ISPRS-J. Photogramm.* **2019**, *148*, 114–129. [CrossRef]
4. Mao, F.J.; Li, P.H.; Zhou, G.M.; Du, H.Q.; Xu, X.J.; Shi, Y.J.; Mo, L.F.; Zhou, Y.F.; Tu, G.Q. Development of the BIOME-BGC model for the simulation of managed Moso bamboo forest ecosystems. *J. Environ. Manag.* **2016**, *172*, 29–39. [CrossRef] [PubMed]
5. Zhang, F.P.; Hou, Y.M.; You, M.S. Effects of different management measures on the composition and structure of arthropod community in *Phyllostachys heterocycla* cv. pubescens forest. *Acta Entomol. Sin.* **2005**, *48*, 928–934. [CrossRef]
6. Chen, D.L.; Wang, B.Y. Life history of *Pantana phyllostachysae* and relationships between the insect and meteorological conditions. *J. Zhejiang For. Coll.* **1993**, *10*, 342–345.
7. Lan, S.W.; Ye, X.Y.; Li, T.S.; Lu, S.Q.; Yang, Z.W.; Lu, M.Z. Type of distribution and method of density estimation for *Pantana phyllostachysae*. *For. Res.* **1993**, *6*, 579–582.
8. Senf, C.; Seidl, R.; Hostert, P. Remote sensing of forest insect disturbances: Current state and future directions. *Int. J. Appl. Earth Obs.* **2017**, *60*, 49–60. [CrossRef]
9. Ye, S.; Rogan, J.; Zhu, Z.; Hawbaker, T.J.; Hart, S.J.; Andrus, R.A.; Meddens, A.J.H.; Hicke, J.A.; Eastman, J.R.; Kulakowski, D. Detecting subtle change from dense Landsat time series: Case studies of mountain pine beetle and spruce beetle disturbance. *Remote Sens. Environ.* **2021**, *263*, 112560. [CrossRef]
10. Aldea, M.; Hamilton, J.G.; Resti, J.P.; Zangerl, A.R.; Berenbaum, M.R.; DeLucia, E.H. Indirect effects of insect herbivory on leaf gas exchange in soybean. *Plant Cell Environ.* **2005**, *28*, 402–411. [CrossRef]
11. Liu, J.; Chen, H.; Wang, J.M.; Chen, X.M.; Yang, Z.X.; Liang, J.S. Photosynthetic traits and antioxidative defense responses of *Pinus yunnanensis* after joint attack by bark beetles *Tomicus yunnanensis* and *T. minor*. *J. For. Res.* **2018**, *30*, 2031–2038. [CrossRef]
12. Pilipović, A.; Drekić, M.; Stojnić, S.; Nikolić, N.; Trudić, B.; Milović, M.; Poljaković-Pajnic, L.; Borišev, M.; Orlović, S. Physiological responses of two pedunculate oak (*Quercus robur* L.) families to combined stress conditions—Drought and herbivore attack. *Sumar. List.* **2020**, *144*, 573–583. [CrossRef]
13. Bárta, V.; Lukeš, P.; Homolová, L. Early detection of bark beetle infestation in Norway spruce forests of Central Europe using Sentinel-2. *Int. J. Appl. Earth Obs.* **2021**, *100*, 102335. [CrossRef]
14. Bhattarai, R.; Rahimzadeh-Bajgiran, P.; Weiskittel, A.; Meneghini, A.; MacLean, D.A. Spruce budworm tree host species distribution and abundance mapping using multi-temporal Sentinel-1 and Sentinel-2 satellite imagery. *ISPRS-J. Photogramm.* **2021**, *172*, 28–40. [CrossRef]
15. Periasamy, S. Significance of dual polarimetric synthetic aperture radar in biomass retrieval: An attempt on Sentinel-1. *Remote Sens. Environ.* **2018**, *217*, 537–549. [CrossRef]
16. Soudani, K.; Delpierre, N.; Berveiller, D.; Hmimina, G.; Vincent, G.; Morfin, A.; Dufrêne, É. Potential of C-band Synthetic Aperture Radar Sentinel-1 time-series for the monitoring of phenological cycles in a deciduous forest. *Int. J. Appl. Earth Obs.* **2021**, *104*, 102505. [CrossRef]
17. Ortiz, S.; Breidenbach, J.; Kändler, G. Early detection of bark beetle green attack using TerraSAR-X and RapidEye data. *Remote Sens.* **2013**, *5*, 1912–1931. [CrossRef]
18. Li, L.W.; Li, N.; Zang, Z.; Lu, D.S.; Wang, G.X.; Wang, N. Examining phenological variation of on-year and off-year bamboo forests based on the vegetation and environment monitoring on a New Micro-Satellite (VENμS) time-series data. *Int. J. Remote Sens.* **2020**, *42*, 2203–2219. [CrossRef]
19. Chen, S.L.; Jiang, H.; Cai, Z.J.; Zhou, X.L.; Peng, C.H. The response of the net primary production of Moso bamboo forest to the On and Off-year management: A case study in Anji County, Zhejiang, China. *Forest Ecol. Manag.* **2018**, *409*, 1–7. [CrossRef]
20. Xu, X.; Du, H.; Zhou, G.; Mao, F.; Li, X.; Zhu, D.; Li, Y.; Cui, L. Remote estimation of canopy leaf area index and chlorophyll content in Moso bamboo (*Phyllostachys edulis* (Carriere) J. Houz.) forest using MODIS reflectance data. *Ann. For. Sci.* **2018**, *75*, 33. [CrossRef]

21. Huang, X.Y.; Xu, Z.H.; Yang, X.; Shi, J.M.; Hu, X.Y.; Ju, W.M. Monitoring the severity of *Pantana phyllostachysae* Chao on bamboo using leaf hyperspectral data. *Remote Sens.* **2021**, *13*, 4146. [CrossRef]
22. Filipponi, F. Sentinel-1 GRD preprocessing workflow. *Proceedings* **2019**, *18*, 11. [CrossRef]
23. Brodu, N. Super-resolving multiresolution images with band-independent geometry of multispectral pixels. *IEEE Trans. Geosci. Remote* **2017**, *55*, 4610–4617. [CrossRef]
24. Goswami, J.; Tajo, L.; Sarma, K.K. Bamboo resources mapping using satellite technology. *Curr. Sci.* **2010**, *99*, 650–653.
25. Qi, S.; Song, B.; Liu, C.; Gong, P.; Luo, J.; Zhang, M.; Xiong, T. Bamboo forest mapping in China using the dense Landsat 8 image archive and Google Earth Engine. *Remote Sens.* **2022**, *14*, 762. [CrossRef]
26. Bagheri, N. Application of aerial remote sensing technology for detection of fire blight infected pear trees. *Comput. Electron. Agric.* **2020**, *168*, 105147. [CrossRef]
27. Guo, Y.K.; Zhang, X.J.; Xu, M.; Liu, Y.L.; Qian, J.; Zhang, Q. Estimation model of equivalent water thickness in the road area. *J. Geo-Inf. Sci.* **2020**, *22*, 308–315. [CrossRef]
28. Jiang, F.G.; Sun, H.; Li, C.J.; Ma, K.S.; Chen, S.; Long, J.P.; Ren, L.X. Retrieving the forest aboveground biomass by combining the red edge bands of Sentinel-2 and GF-6. *Acta Ecol. Sin.* **2021**, *41*, 8222–8236. [CrossRef]
29. Blaes, X.; Defourny, P.; Wegmuller, U.; Della Vecchia, A.; Guerriero, L.; Ferrazzoli, P. C-band polarimetric indexes for maize monitoring based on a validated radiative transfer model. *IEEE T. Geosci. Remote* **2006**, *44*, 791–800. [CrossRef]
30. Nasirzadehdizaji, R.; Balik Sanli, F.; Abdikan, S.; Cakir, Z.; Sekertekin, A.; Ustuner, M. Sensitivity analysis of multi-temporal sentinel-1 SAR parameters to crop height and canopy coverage. *Appl. Sci.* **2019**, *9*, 655. [CrossRef]
31. Yan, K.; Zhang, D. Feature selection and analysis on correlated gas sensor data with recursive feature elimination. *Sens. Actuators B-Chem.* **2015**, *212*, 353–363. [CrossRef]
32. Chen, T.Q.; Guestrin, C. XGBoost: A scalable tree boosting system. In Proceedings of the 22nd ACM SIGKDD International Conference on Knowledge Discovery and Data Mining (KDD), San Francisco, CA, USA, 13 August 2016; pp. 785–794.
33. Cao, Z.G.; Ma, R.H.; Melack, J.M.; Duan, H.T.; Liu, M.; Kutser, T.; Xue, K.; Shen, M.; Qi, T.C.; Yuan, H.L. Landsat observations of chlorophyll-a variations in Lake Taihu from 1984 to 2019. *Int. J. Appl. Earth Obs.* **2022**, *106*, 102642. [CrossRef]
34. Xie, B.Q.; Ding, J.L.; Ge, X.Y.; Li, X.H.; Han, L.J.; Wang, Z. Estimation of soil organic carbon content in the Ebinur Lake wetland, Xinjiang, China, based on multisource remote sensing data and ensemble learning algorithms. *Sensors* **2022**, *22*, 2685. [CrossRef]
35. Chawla, N.V.; Bowyer, K.W.; Hall, L.O.; Kegelmeyer, W.P. SMOTE: Synthetic minority over-sampling technique. *J. Artif. Intell. Res.* **2002**, *16*, 321–357. [CrossRef]
36. Sandberg, G.; Soja, M.J.; Ulander, L.M.H. Impact and modeling of topographic effects on P-band SAR backscatter from boreal forests. In Proceedings of the IEEE International Geoscience and Remote Sensing Symposium (IGARSS), Vancouver, BC, Canada, 24–29 July 2011; pp. 3522–3525.
37. Li, L.W.; Li, N.; Lu, D.S.; Chen, Y.Y. Mapping Moso bamboo forest and its on-year and off-year distribution in a subtropical region using time-series Sentinel-2 and Landsat 8 data. *Remote Sens. Environ.* **2019**, *231*, 111265. [CrossRef]
38. Li, X.J.; Du, H.Q.; Zhou, G.M.; Mao, F.J.; Zhang, M.; Han, N.; Fan, W.L.; Liu, H.; Huang, Z.H.; He, S.B.; et al. Phenology estimation of subtropical bamboo forests based on assimilated MODIS LAI time series data. *ISPRS-J. Photogramm.* **2021**, *173*, 262–277. [CrossRef]
39. Meng, R.; Dennison, P.E.; Zhao, F.; Shendryk, I.; Rickert, A.; Hanavan, R.P.; Cook, B.D.; Serbin, S.P. Mapping canopy defoliation by herbivorous insects at the individual tree level using bi-temporal airborne imaging spectroscopy and LiDAR measurements. *Remote Sens. Environ.* **2018**, *215*, 170–183. [CrossRef]
40. Xu, Z.; Zhang, Q.; Xiang, S.; Li, Y.; Huang, X.; Zhang, Y.; Zhou, X.; Li, Z.; Yao, X.; Li, Q.; et al. Monitoring the severity of *Pantana phyllostachysae* Chao infestation in Moso bamboo forests based on UAV multi-spectral remote sensing feature selection. *Forests* **2022**, *13*, 418. [CrossRef]